

# High Resolution VLBI Astrometry with the $\theta$ - $\theta$ Transform

Daniel Baker,<sup>1,2\*</sup> Walter Brisken,<sup>3</sup> Marten H. van Kerkwijk,<sup>4</sup> Rik van Lieshout<sup>1</sup> Ue-Li Pen,<sup>1,4</sup>

<sup>1</sup>Canadian Institute for Theoretical Astrophysics, University of Toronto, 60 St. George Street, Toronto, ON M5S 3H8, Canada

<sup>2</sup>Department of Physics, University of Toronto, 60 St. George Street, Toronto, ON M5S 1A7, Canada

<sup>3</sup>National Radio Astronomy Observatory, Socorro, NM 87801, USA

<sup>4</sup>Department of Astronomy and Astrophysics, University of Toronto, 50 St. George Street, Toronto, ON M5S 3H4, Canada

Accepted XXX. Received YYY; in original form ZZZ

## ABSTRACT

The recent development of  $\theta$ - $\theta$  techniques in pulsar scintillometry has opened the door for new high resolution imaging techniques of the scattering medium. By solving the phase retrieval problem and recovering the wavefield from a pulsar dynamic spectrum, the Doppler shift, time delay, and phase offset of individual images can be determined. However, the results of phase retrieval from a single dish are only know up to a constant phase rotation, which prevents their use for astrometry using Very Long Baseline Interferometry. We present an extension to previous  $\theta$ - $\theta$  methods using the interferometric visibilities between multiple stations to calibrate the wavefields. When applied to existing data for PSR B0834+06 we measure the effective screen distance and lens orientation with five times greater precision than previous works.

**Key words:** keyword1 – keyword2 – keyword3

## 1 INTRODUCTION

Scattering of radio emission by the Interstellar Medium (ISM) is a general nuisance to the radio astronomy community. For imaging experiments such as the Event Horizon Telescope (EHT) it leads to distortions of the final image (Zhu et al. 2019). For Pulsar Timing Arrays (PTAs), it increases timing noise and can even masquerade as a gravitational wave signal (Main et al. 2020). In order to escape these problems, PTAs use high frequency observations where the effects of scattering are reduced. However, pulsar brightness falls off at higher frequencies and so the removal of scattering effects comes at the cost of the number of pulsars available for the array. An understanding of scattering structures in the ISM, particularly those affecting pulsars, would be a boon to the field. Fortunately, pulsar observations provide an excellent source of information about the ISM. As effectively point sources, pulsars exhibit scintillation behaviour that allows us to probe small scale structure in the ISM. Variations in free electron density result in the formation of multiple images of the pulsar on the sky whose interference pattern can be observed. The standard representation of this phenomenon is the observed intensity as a function of both time and frequency known as the dynamic spectrum. Originally believed to be the result of turbulence in the ISM, our understanding of pulsar scintillation underwent a fundamental shift with the discovery of parabolic scintillation arcs by Stinebring et al. (2001). These features are seen in the 2D Fourier transform of the dynamic spectrum, known as the conjugate spectrum, or its magnitude squared, known as the secondary spectrum; and are indicative of the lensed images falling along a linear feature in the sky. In some systems, the main parabolic arc can be seen to consist of a collection of inverted arclets of the same curvature extending

downwards from points on the main parabola. Points along the main parabola are interpreted as the interference of scattered images with a "line of sight" image, while the inverted arclets are caused by the interference of pairs of scattered images.

One proposal for the source of these parabolic structures is corrugated reconnection sheets (Pen & Levin 2014). These structures are expected to exist along magnetic domain boundaries in the ISM and support surface waves. When the sheet is nearly aligned with the line of sight to the pulsar, grazing light at wave crests will be strongly refracted. If the sheet possesses multiple crests, the resulting images will appear nearly linear on the sky analogously to light reflecting off a wavy lake. Simard & Pen (2018) expand on this model to predict the evolution of these images over both time and frequency.

In order to test this model, one would like to produce high resolution astrometric images of the screen. For PSR B0834+06, this has been achieved by Brisken et al. (2010) using very-long-baseline interferometry (VLBI) measurements to produce  $100\mu\text{as}$  resolution images of the screen. Since the points in the conjugate spectrum along the main arc, or alternatively the apexes of the inverted arclets, represent the interference of images with the line of sight, their phases encode information about their angular offset. The first step in forming an image is to identify these points in the conjugate spectrum. Since the inverted arclets are extended, and may be densely packed, this identification is nontrivial. By solving the phase retrieval problem and restoring the underlying wavefield at each dish, individual images can be identified as isolated points in its Fourier transform: the conjugate wavefield.

The first application of a method for solving the phase retrieval problem in pulsar scintillometry is presented in Walker & Stinebring (2005). This approach iteratively adds new images to the the conjugate wavefield to build up an approximate solution similar to the CLEAN algorithm. However, the invention of the  $\theta$ - $\theta$  transform by

\* E-mail: dbaker@cita.utoronto.ca

Sprenger et al. (2020) opens up a new approach to phase retrieval. Under the assumption of a one dimensional lens, this transformation maps the conjugate spectra into a space where the inverted arcslets form a grid of horizontal and vertical lines. Baker et al. (2021) show how the complex magnifications of each image can be found using the eigenvectors of the transformed spectrum and how these can be mapped back to reproduce the wavefield. Unfortunately, since phases recovered using a single dish can only be found up to some unknown phase rotation as rotating a solution by any constant phase will leave the dynamic spectrum unchanged, the relative phases of dishes cannot be determined using these methods. This precludes their use for measuring the geometry of the lens.

In this paper we present a method for using the additional information contained in the visibilities from VLBI observations to fix the relative phases of the recovered wavefields and allow for astrometric imaging, and demonstrate its use on the observation of B0834+06 of Briskeen et al. (2010). This data is particularly interesting as the presence of two discrete collections of images, a traditional scintillation arc and a collection of arcslets offset from that main arc at a time delay of approximately 1 ms, suggests lensing by multiple screens. The theory behind this technique is described in Sec. 2. In Sec. 3 we describe the observations used to test this method as well as their preparation for analysis. In Sec. 4 we discuss the recovered wavefields. In Sec. 5 we show how the geometry of the lenses, including effective distances, can be determined. Finally, Sec. 6 presents an astrometric image produced from our analysis

## 2 VLBI WITH $\theta-\theta$

For single dish observations,  $\theta-\theta$  methods have been shown to be able to recover the wavefields underlying pulsar dynamic spectra. However, since this amounts to undoing the convolution of the wavefield with itself there is an unknown overall phase rotation in the result. Since interferometry relies on the relative phases between stations, it is insufficient to independently recover the fields for each station. In order to avoid the problem we must simultaneously perform the recovery at all stations and include information about their relative phases. To this end, we consider the visibility between any two stations. A breakdown of the quantities discussed in this approach is shown in Table 1, which serves as an extension of the table in Simard et al. (2019). For dynamic wavefields at the two stations  $W_i(\nu, t)$  and  $W_j(\nu, t)$ , the visibility is given by

$$V_{i,j}(\nu, t) = W_i(\nu, t) W_j^*(\nu, t) \quad (1)$$

and so, denoting Fourier transforms with a tilde,

$$\tilde{V}_{i,j}(\tau, f_D) = \tilde{W}_i(\tau, f_D) * \tilde{W}_j^*(-\tau, -f_D) \quad (2)$$

where  $f_D$  and  $\tau$  are the conjugate variables to time and frequency respectively, and  $\tilde{W}_i$  and  $\tilde{W}_j$  are the conjugate wavefields. For each dish, the conjugate spectrum is given by the convolution

$$\tilde{I}_i(f_D, \tau) = \tilde{W}_i(f_D, \tau) * \tilde{W}_i^*(-f_D, -\tau) \quad (3)$$

or in  $\theta-\theta$  space as the outer product

$$\mathbf{l}_i = \boldsymbol{\mu}_i \otimes \boldsymbol{\mu}_i \quad (4)$$

where  $\boldsymbol{\mu}_i$  is the complex response vector giving the magnification and phase rotation of points along the lens as described in Baker et al. (2021). Similarly, the visibility in the  $\theta-\theta$  space becomes

$$\mathbf{V}_{i,j} = \boldsymbol{\mu}_i \otimes \boldsymbol{\mu}_j \quad (5)$$

It follows that most of the information for the magnifications from each dish can be recovered from the visibility alone. To demonstrate

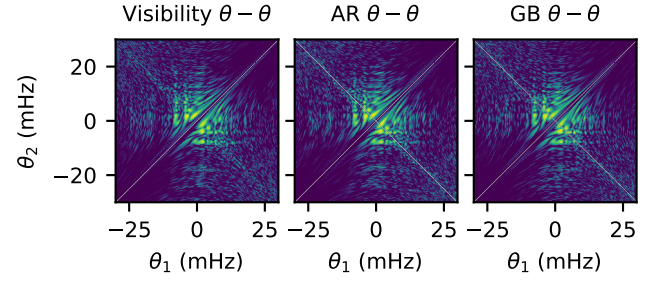


**Figure 1.** Amplitudes of the  $\theta-\theta$  spectra from the same portion of the data from dynamic spectra of Arecibo and Green Bank as well as the visibility between the two.

this, we consider a simultaneous chunk of data from the Arecibo (AR) and Green Bank (GB) dynamic spectra (see 3 as well as their visibility. Using the fitted curvature for the parabolic arc as described in Baker et al. (2021), we generate their  $\theta-\theta$  spectra in Fig. 1 Instead of modelling the  $\theta-\theta$  spectra using their dominant eigenvector, we will instead model them using their largest singular value. This takes the form:

$$\mathbf{l}_i = S_i \mathbf{a}_i \otimes \mathbf{b}_i \quad (6)$$

$$\mathbf{V}_{i,j} = S_{i,j} \mathbf{a}_{i,j} \otimes \mathbf{b}_{i,j}$$

where  $\mathbf{a}$  and  $\mathbf{b}$  are vectors and  $S$  is the singular value. Combining this with our definition of the  $\theta-\theta$  spectra for single dishes and visibilities, it follows that

$$\boldsymbol{\mu}_i = \mathbf{a}_i = \mathbf{a}_{i,j} = \mathbf{b}_{j,i}^* \quad (7)$$

It is worth noting at this stage that multiplying  $\mathbf{a}_{i,j}$  while dividing  $\mathbf{b}_{i,j}$  by the same constant will not change our final model. The relative amplitudes of the  $\boldsymbol{\mu}_i$  and  $\boldsymbol{\mu}_j$  cannot be determined from the visibilities alone. As such we restrict ourselves to examining the phases of the magnifications. For our example, the phases of  $\mathbf{a}_{ar}$  and  $\mathbf{a}_{AR,GB}$  should agree up to a constant offset, and similarly for  $\mathbf{a}_{GB}$  and  $\mathbf{b}_{AR,GB}^*$ . Fig 2 shows the difference in phase of the two approaches for each dish. As expected, both dishes are offset by – different– constant phases. This difference arises from the random phase associated with the single dish recoveries since the relative phases between Arecibo and Green Bank are forced by the visibility. In theory, the visibilities alone could be used to determine the relative phases for each baseline in an array one at a time. However, a more elegant solution exists allowing us to find the relative phases and amplitudes at all dishes simultaneously. If we define the concatenated response vector for a VLBI observation with  $n$  stations as

$$\boldsymbol{\mu} = \boldsymbol{\mu}_1 \oplus \boldsymbol{\mu}_2 \oplus \dots \oplus \boldsymbol{\mu}_n \quad (8)$$

then the outer product  $\boldsymbol{\mu} \otimes \boldsymbol{\mu}$  will be given by the block matrix

$$\boldsymbol{\mu} \otimes \boldsymbol{\mu} = \begin{pmatrix} \mathbf{l}_1 & \mathbf{V}_{1,2} & \dots & \mathbf{V}_{1,n} \\ \mathbf{V}_{1,2}^\dagger & \mathbf{l}_2 & \dots & \mathbf{V}_{2,n} \\ \vdots & \vdots & \ddots & \vdots \\ \mathbf{V}_{1,n}^\dagger & \mathbf{V}_{2,n}^\dagger & \dots & \mathbf{l}_n \end{pmatrix} \quad (9)$$

We can now recover  $\boldsymbol{\mu}$ , as for the single dish case, by taking the dominant eigenvector. The unknown phase rotation for the individual  $\boldsymbol{\mu}_i$  is now held fixed, and the relative phases can be determined.

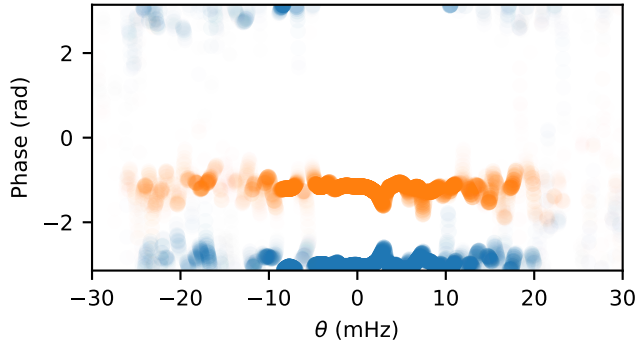


**Figure 2.** Relative phase between the magnifications measured on a single dish and from the visibility for Arecibo (blue) and Green Bank (orange). The transparency of each point shows the amplitude relative to the peak magnification for each dish. Both dishes show constant (and unrelated) phase offsets between the two methods due to the non uniqueness of the  $\theta$ - $\theta$  solution under phase rotations.

**Table 1.** Definitions of common quantities in scintillometry using VLBI and their relations to the wavefield.

Parameter	Symbol	Description
Single Dish Quantities		
Dynamic wavefield	$W_i(\nu, t)$	The impulse response function of the interstellar medium between the source and antenna i.
Dynamic spectrum	$I_i(\nu, t) =  W_i(\nu, t) ^2$	The observed intensity of the pulsar at station i, at frequency $\nu$ and time $t$ .
Conjugate wavefield	$\widetilde{W}_i(\tau, f_D)$	The Fourier transform of the dynamic wavefield for station i.
Conjugate spectrum	$\widetilde{I}_i(\tau, f_D) = (\widetilde{W}_i * \widetilde{W}_i^*)(\tau, f_D)$	The Fourier transform of the dynamic spectrum at station i.
Secondary spectrum	$S_{Ii,i}(\tau, f_D) =  \widetilde{I}_i(\tau, f_D) ^2$	The auto-correlation of the dynamic spectrum station i with itself.
VLBI Quantities		
Cross conjugate wavefield	$S_{W_{i,j}}(\tau, f_D) = \widetilde{W}_i(\tau, f_D) \widetilde{W}_j^*(\tau, f_D)$	The cross-correlation of the dynamic wavefields at stations i and j, in the Fourier domain.
Intensity cross secondary spectrum	$S_{I_{i,j}}(\tau, f_D) = \widetilde{I}_i(\tau, f_D) \widetilde{I}_j^*(\tau, f_D)$	The cross-correlation of the dynamic spectra at stations i and j, in the Fourier domain.
Visibility dynamic cross-spectrum	$V_{i,j}(\nu, t) = W_i(\nu, t) W_j^*(\nu, t)$	The visibility of the pulsar between stations i and j at frequency $\nu$ and time $t$ .
Visibility conjugate spectrum	$\widetilde{V}_{i,j}(\tau, f_D) = (\widetilde{W}_i * \widetilde{W}_j^*)(\tau, f_D)$	The Fourier transform of the visibility between stations i and j.
Visibility secondary cross-spectrum	$S_{V_{i,j}}(\tau, f_D) = \widetilde{V}_{i,j}(\tau, f_D) \widetilde{V}_{i,j}^*(-\tau, -f_D)$	Sensitive to the sum of the angular separations of images from the pulsar.

### 3 DATA

For a test case we use data taken for PSR B0834+06 by [Briskin et al. \(2010\)](#) in 2005. Data was taken simultaneously using Arecibo (AR), the Green Bank Telescope (GB), Jodrell Bank (JB), and tied-array Westerbork (WB). Visibilities and dynamic spectra with 244 Hz frequency resolutions and 1.25 s integrations were created for a 32 MHz band centered around 316.5 MHz and 110 minutes of simultaneous observation with the DiFX software correlator. Unfortunately, calibration issues with the WB data prevented its use, and only AR,GB, and JB were included in this analysis.

#### 3.1 Normalization

In order to use the composite  $\theta$ - $\theta$  method the data from different stations has to be renormalized. The first step is to apply a singular value decomposition (SVD) on each dynamic spectrum in order to divide out pulse to pulse variation and the band pass and set the mean to unity. Since the eigenvalue decomposition of the  $\theta$ - $\theta$  matrix assumes uniform noise the dynamic spectra are then rescaled to have the same noise as the highest signal to noise spectrum (the Arecibo dynamic spectrum in this case). To do this, noise is measured in the secondary spectra using points far from the main arc. Each dynamic spectrum is then divided by the ratio of its noise to the reference spectrum. However, this also rescales the magnification vector for each dynamic spectrum. Since these vectors must be consistent between the dynamic spectra and visibilities, the visibilities must also be rescaled. As for the dynamic spectra, an SVD is used to remove pulse to pulse variation and the band pass. The SVD can also be used to correct lingering phase calibration issues in the visibility by removing large scale phase structures such that the average phase over many scintles is zero. Finally, each visibility is rescaled such the mean of its amplitude squared is equal to the mean of the product of the corresponding dynamic spectra.

### 4 VLBI PHASE RETRIEVAL OF B0834+06

The method for phase retrieval in the VLBI case remains much the same as for the single dish case. First, the data is divided into a series of chunks consisting of 10.5 minutes of data over 0.125MHz chosen such that each chunk overlaps halfway in time and or frequency with the chunks around it. Next, the measured curvature of  $5.401 \pm .003s^3$  at 320MHz from [Baker et al. \(2021\)](#) is scaled to the mean frequency of the chunk and used to generate  $\theta$ - $\theta$  spectra for each dynamic spectrum and visibility. The  $\theta$ - $\theta$  spectra from each individual dish and baseline are then combined into a single block matrix as described in Sec. 2. An example of this using the two highest signal to noise dishes (Arecibo and Green Bank) is shown in Fig. 3. The dominant eigenvector of this matrix gives an estimate of the concatenated response vector defined in Eq. 8. The outer product of  $\mu$  with itself is shown in the middle pannel of Fig. 3 for comparison purposes. The concatenated response is then broken up into the response vectors of the individual dishes. These are then mapped back into time-frequency space and the results from all chunks are combined using the mosaic approach described in [Baker et al. \(2021\)](#). Briefly, the wavefield  $W_n$  within each chunk is added successively to the full wavefield  $W$  such that within the overlapping region

$$\arg(\langle WW_n^* \rangle) = 0 \quad (10)$$

However, to make sure that phases remain consistent between the dishes, we now used the weighted average of the overlapping regions

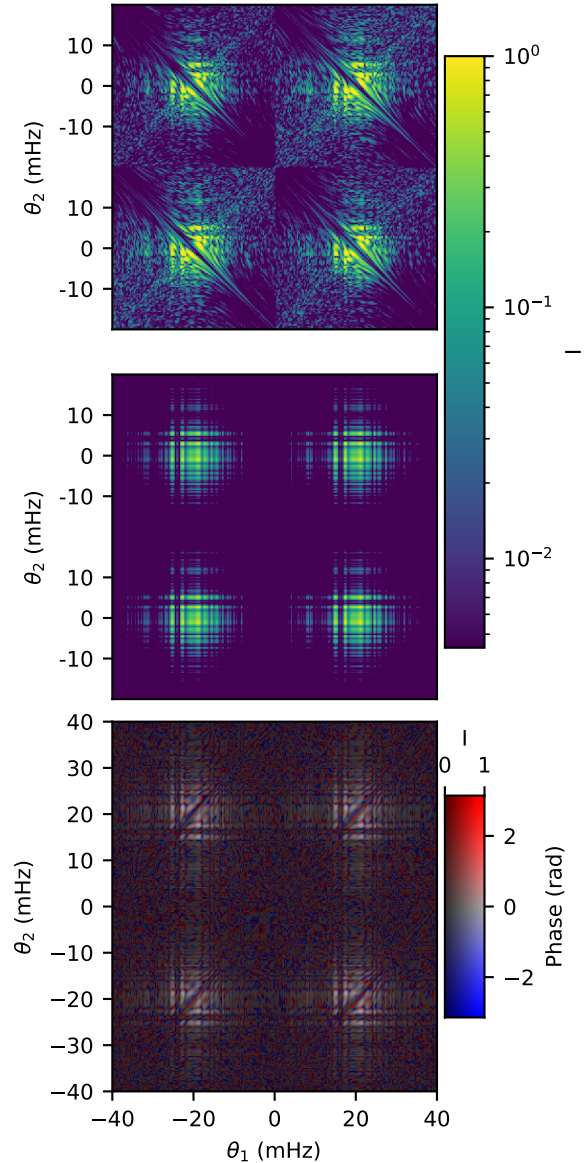


**Figure 3.** Magnitude squared of Data (top) and Model (middle)  $\theta$ - $\theta$  spectra, as well as the phase difference between the two (bottom), for two station VLBI with Arecibo and Green Bank telescopes. For the phase difference, phases are shown by colour and Intensity relative to the max in saturation. Clockwise from top left the blocks of the matrix are made from the Arecibo dynamic spectrum, the visibility between the two stations, the Green Bank dynamic spectrum, and the complex conjugate of the visibility.

at all dishes to determine the phase rotation when adding a new section. A portion of the dynamic spectra produced from the recovered wavefields using this method on AR,GB, and JB are show in Fig. 4. For comparison purposes we also include the results from single dish recovery at each station. Many features of the JB wavefield that were lost due the lower signal to noise of the dynamic spectrum are recovered through the information in the visibilities.

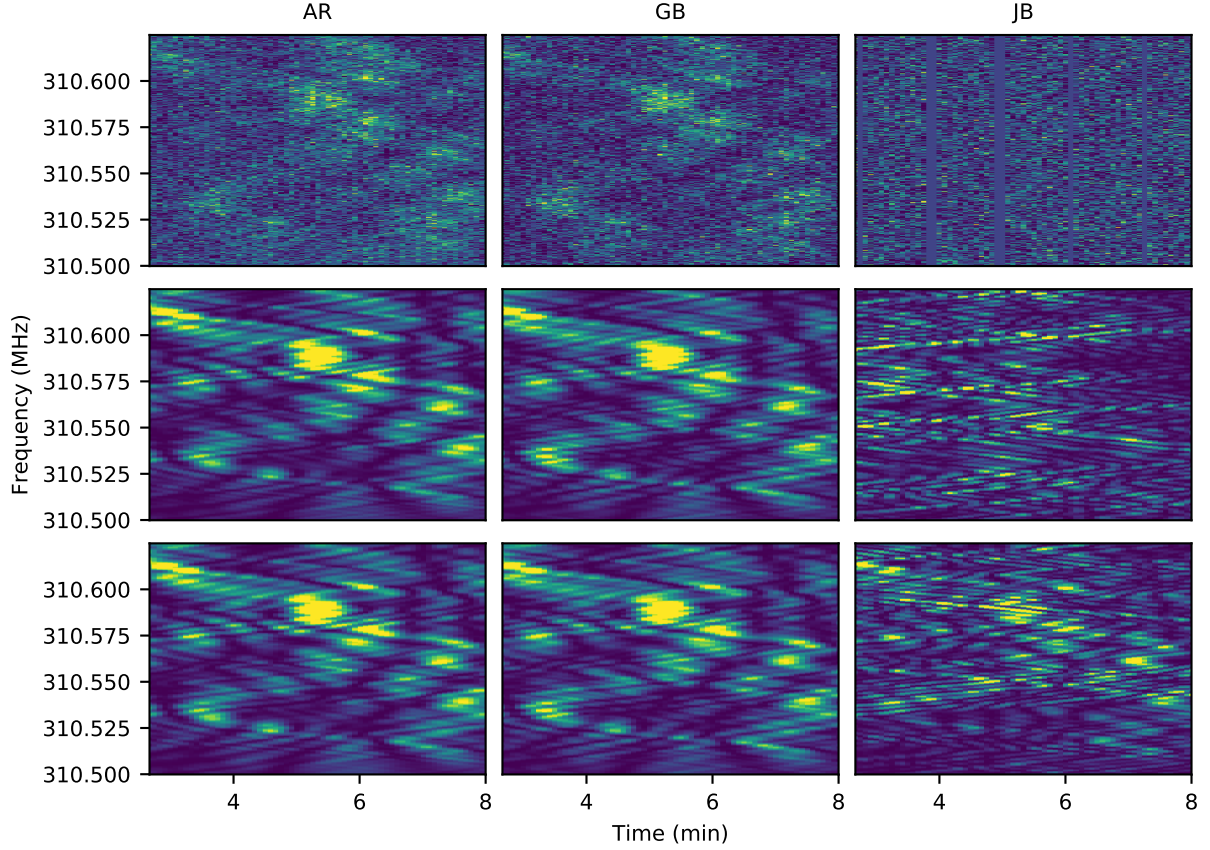


**Figure 4.** Comparison of the measured dynamic spectra (top) to the single dish (middle), and VLBI (bottom) models for three dishes. The extra information in the visibilities yields a marked improvement in the JB recovery.

## 5 LENS PARAMETERS

Since the main arc and millisecond feature appear distinct in the conjugate wavefield, we address the question of whether they come from distinct screens on the sky. We begin by modelling the main arc as a single line of images located at some effective distance  $d_{\text{eff},1}$  and rotated by an angle  $\Omega_1$  east of the declination axis. For an image with a given time delay  $\tau$ , its angular offset is given by

$$|\theta| = \sqrt{\frac{2c\tau}{d_{\text{eff},1}}} \quad (11)$$

Since the sign of  $f_D$  for an image determines which side of the line of sight it lies along the line of images, we use this to specify the side of the lens with

$$\theta(f_D, \tau) = \pm \text{sgn}(f_D) \sqrt{\frac{2c\tau}{d_{\text{eff},1}}} \quad (12)$$

the choice of  $\pm$  will define which direction along the screen is positive and will rotate the value of  $\Omega_1$  by 180 deg. We have chosen the  $-$  convention as this gives a position angle between 0 and 180 deg. For a given projected baseline  $\mathbf{b}$  onto the sky towards the pulsar observed at wavelength  $\lambda$ , the phase,  $\phi$  of the corresponding cross conjugate wavefield for an image with Doppler frequency  $f_D$  along the main arc is given, assuming the angular offset of the image is small, by

$$\phi(f_D) = -2\pi \left[ f_D \mathbf{b} \cdot \mathbf{s}_1 \sqrt{\frac{2c\eta}{d_{\text{eff},1}}} \right] \lambda^{-1} \quad (13)$$

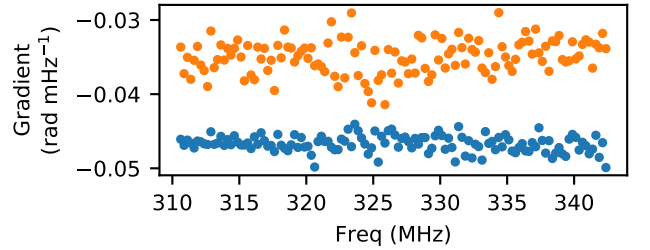


**Figure 5.** Best fit phase gradients using 0.25 MHz subbands of the ARGB (blue) and ARJB (orange) baselines.

where  $\mathbf{s}_1$  is the unit vector along the screen. Which gives us a constant phase gradient over  $f_D$  when our angular offsets are small (as is the case here) of  $-2\pi \mathbf{b} \cdot \mathbf{s}_1 \sqrt{\frac{2c\eta}{d_{\text{eff},1}}} \lambda^{-1}$ . If we rotate the cross conjugate wavefield for this baseline by  $-\phi(f_D)$ , the signal should become entirely real and so the imaginary part will be entirely noise. Hence, our best fit gradient is the one that minimizes the sum of the squares of the imaginary part when used to derotate the data. The best fit phase gradients using 128 subbands of 0.25 MHz are shown in Fig. 5. The average gradients for the two baselines are  $-0.0479 \pm 0.0001$  rad  $\text{mHz}^{-1}$  for ARGB and  $-0.0350 \pm 0.0002$  rad  $\text{mHz}^{-1}$  for ARJB. Together, these imply an effective distance of  $d_{\text{eff},1} = 1.186 \pm 0.005$  kpc and position angle of  $\Omega_1 = 155.0 \pm 0.1^\circ$

As previously observed in [Briskin et al. \(2010\)](#), the images of the millisecond feature are offset from the main lens the line of images does not intersect our line of sight to the pulsar. As such we include the offset of the line of images as a third parameter in our model. Unlike [Liu et al. \(2016\)](#), our model assumes that each image is the result of lensing by single screen with no doubly lensed images. For a line of images at effective distance  $d_{\text{eff},2}$ , whose closest point to the line of sight is offset from the line of sight by  $\theta_0$  we model the phase difference along a baseline  $\mathbf{b}$  as

$$\phi(\tau) = \pm 2\pi \left( \mathbf{b} \cdot \boldsymbol{\theta}_0 + \sqrt{\frac{2c\tau}{d_{\text{eff},2}} - |\boldsymbol{\theta}_0|^2 (\mathbf{b} \cdot \mathbf{s}_2)} \right) \lambda^{-1} \quad (14)$$

where  $\mathbf{s}_2$  is the unit vector along the lens which is perpendicular to  $\boldsymbol{\theta}_0$ . The sign of the phase will depend on which direction along the lens we define to be positive as well as which side of the closest point the image in question lies on. We define three parameters to describe the phase at closest approach,  $\phi_0$ , phase evolution,  $B$ , and minimal time delay,  $\tau_0$  for the millisecond feature as

$$\phi_0 = \frac{2\pi\boldsymbol{\theta}_0 \cdot \mathbf{b}}{\lambda} \quad (15)$$

$$B = \frac{2\pi\mathbf{s}_2 \cdot \mathbf{b}}{\lambda} \sqrt{\frac{2c}{d_{\text{eff},2}}} \quad (16)$$

$$\tau_0 = \frac{d_{\text{eff},2}}{2c} \theta_0^2 \quad (17)$$

which simplifies Eq. 14 to

$$\phi(\tau) = \pm (\phi_0 + B\sqrt{\tau - \tau_0}) \quad (18)$$

The most important of these parameters for our work are  $\phi_0$ , which gives the relative astrometric position of the closest approach, and  $\tau_0$  which can be combined with the astrometric position to determine effective distance. Using a fixed value of  $\tau_0 = 954.6 \mu\text{s}$  from [Zhu et al. \(in prep\)](#) we fit for the remaining parameters along each baseline by minimizing the sum of the squares of the imaginary parts. Since the millisecond feature is fainter than the main arc, wider frequency bands are used for the fitting in order to increase the signal to noise ratio. The results of these fits for  $\phi_0$  for the sixteen 2 MHz subbands across the observation are show in Fig. 6. The value of  $B$  for the ARGB baseline is consistent with 0 ( $-0.2 \pm 0.3 \text{ rad } \mu\text{s}^{-1/2}$ ), which results in a degenerate solution for  $\phi_0$  offset by  $\pi$ . The two solutions can be distinguished by requiring that the real part of the derotated CCWF be positive where there is signal. Scaling all  $\phi_0$  to 320 MHz and averaging gives final values of  $\phi_0 = 0.73 \pm 0.03 \text{ rad}$  for the ARGB baseline and  $\phi_0 = 3.8 \pm 0.1 \text{ rad}$  for the ARJB baseline. Since the derotation is equally effective with the addition of any multiple of  $2\pi$  to either baseline we have chosen our  $\phi_0$  such that the variance in the astrometric position of the base of the feature across all bands is minimized. Mapping onto the sky give  $d_{\text{eff},2} = 1.41 \pm 0.09 \text{ kpc}$ ,  $\theta_0 = 23.7 \pm .8 \text{ mas}$ , and a position angle towards the closest point of  $\Omega_2 = 37 \pm 1^\circ$ . All errors assume the measured curvature from [Baker et al. \(2021\)](#) is exact since the fractional error of less than 0.01 percent is much smaller than the errors in the phase of the conjugate wavefields.

A simple schematic of the two screens projected onto the sky is shown in Fig. 7. In order to test our model examine the ARGB baseline through different stages of modelling in Fig. 8. A key feature of the data visibility is the crisscross pattern of features in the imaginary part. The negative features, running down and to the right, and the positive features, running down and to the left, come from features on different sides of the parabola in the conjugate spectrum. The

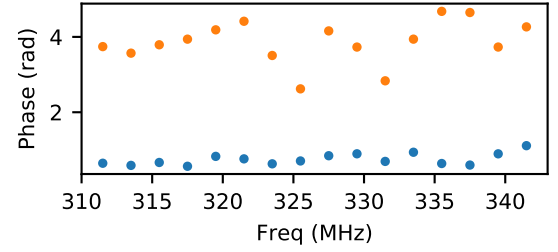


**Figure 6.** Fitted values of the phase at the base of the millisecond feature using a fixed  $\tau_0$  for ARGB (blue) and ARJB (orange) baselines. The phases of the ARJB baseline have been corrected by  $\pi$  whenever the degenerate solution was found.

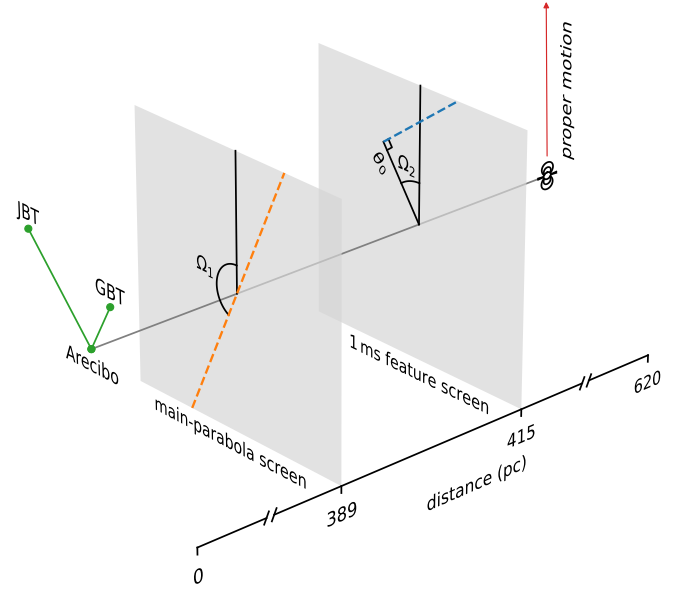


**Figure 7.** A simple schematic of the two screens. The dotted orange line indicates the orientation of the main screen, while the blue line shows the lens responsible for the millisecond feature. Since features are only seen on one side of the closest point we only show that side of the millisecond lens. The angles  $\Omega$  and  $\Omega_2$  as well as the closest offset  $\theta_0$  used to define the lenses are also shown. Green lines show the two baselines used in our analysis. Distances are shown assuming the fiducial pulsar distance of 620 pc

signs of the crisscross are due to the time delay between the dishes. If we can correctly model this delay, we should be able to remove the imaginary features and leave only the real part. At that point, we have extracted all the new information from VLBI and are left with only the dynamic spectrum. Initially, these features are also quite clear in the  $\theta$ - $\theta$  model of the visibility, which is a good indication of its success at capturing the data. Using the five parameter fit described above, we can derotate the Green Bank conjugate wavefield to remove the effects of the time delays to different images relative to Arecibo. Transforming back to a wavefield and generating a new model visibility with Arecibo removes much of the imaginary structure. This also allows us to see how the model affects the phase at each point in the visibility. Applying the same change of phase to the raw data also removes most of the imaginary part.

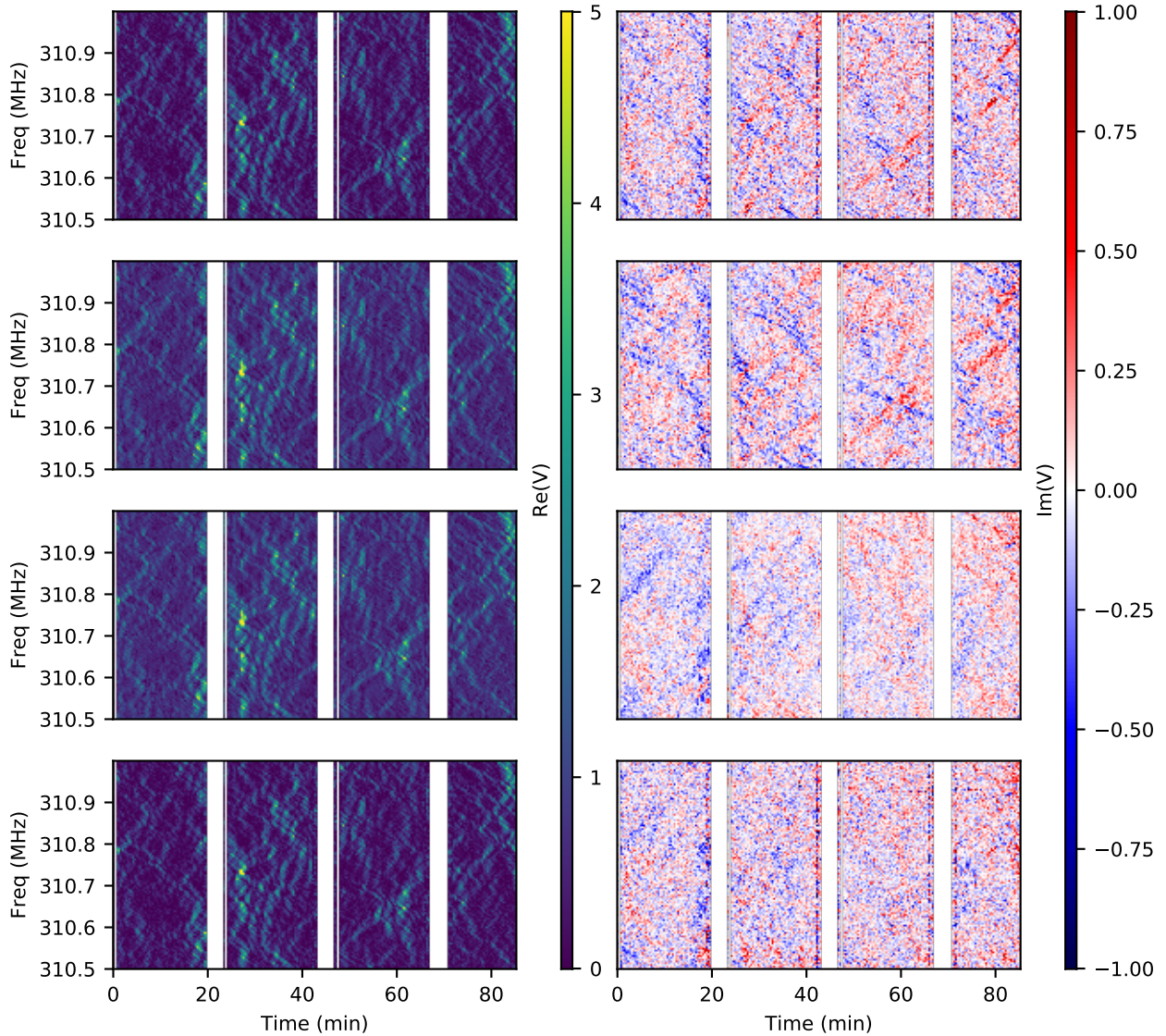


**Figure 8.** Sample region of the real (left) and imaginary (right) parts of ARGV visibility during different stages of modelling. The raw data (top) and  $\theta$ - $\theta$  model (second from top) show a clear crisscross structure due to power on different sides of the parabola. After correcting for the phase difference between the dishes from our five parameter model (second from bottom) most of this structure is removed. Finally, the same phase difference is applied to the raw data (bottom) and we see that our model is able to account for almost all of the imaginary structure.

### 5.1 Examining Residuals

After removing the phase gradient from our best fit physical parameters, we can look for areas in the cross conjugate wavefield or its  $\theta$ - $\theta$  transform that deviate from the model. Since signals are more dispersed in the conjugate spectrum than the conjugate wavefield, it is easier to locate these small deviations. As discussed [Baker et al. \(2021\)](#), a small feature can be seen to branch from the main arc at approximately  $300 \mu\text{s}$  on the negative Doppler side of the arc. Examining this feature in  $\theta$ - $\theta$  after the removal of our model phase gradient, we see, in [Fig. 9](#), that there exists some residual phase offset on the feature on the ARGV baseline. Since this feature is at the same time delay as the main arc, this phase offset may indicate a slightly different distance. Unfortunately, the ARJB baseline is too noisy in this region to allow us to properly map the feature to determine its distance.

**Table 2.** Measured and inferred parameters for the main and millisecond feature lenses.

Parameter	Value
Measured (Scaled to 320 MHz)	
ARGB Main Arc Gradient (rad mHz <sup>-1</sup> )	-0.0467 ± 0.0001
ARJB Main Arc Gradient (rad mHz <sup>-1</sup> )	-.0350 ± 0.0002
$\phi_{0,ARGB}$ (rad)	0.73 ± 0.03
$\phi_{0,ARJB}$ (rad)	3.8 ± 0.1
Inferred	
$d_{\text{eff},1}$ (kpc)	1.186 ± .005
$d_{\text{eff},2}$ (kpc)	1.41 ± .09
$\Omega_1$ (deg)	155.0 ± 0.1
$\Omega_2$ (deg)	37 ± 1
$\theta_0$ (mas)	23.7 ± .8

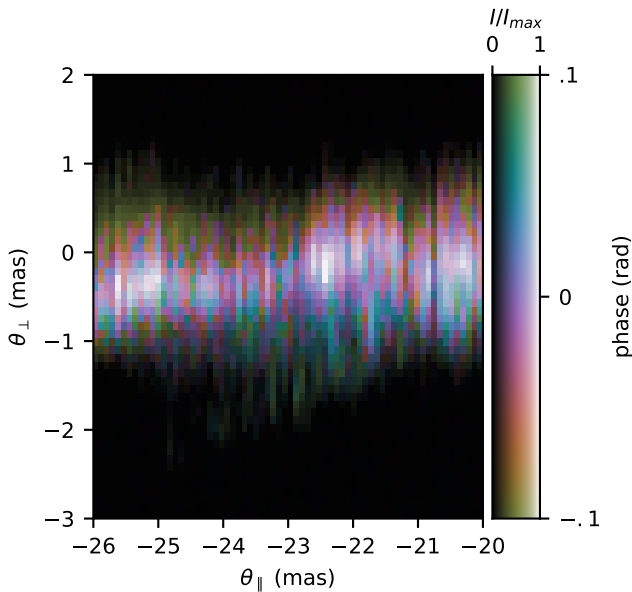


**Figure 9.** Phase of the  $\theta$ - $\theta$  matrix near the 300  $\mu$ s feature after removing our best fit model with lightness used to indicate relative intensity.

## 6 ASTROMETRIC IMAGING

In addition to the general lens parameters described above, VLBI  $\theta$ - $\theta$  methods also allow for high precision relative astrometry of the lens. In particular, we are able to search for any deviations from our one dimensional model. By applying the  $\theta$ - $\theta$  transformation to the recovered cross conjugate wavefield for ARGB in 2MHz bands, after rescaling  $f_D$  to correct curvatures to 320 MHz, and averaging over all subbands, we create a map of the image positions in coordinates parallel and perpendicular to the major axis of the screen. Since the  $\theta$ - $\theta$  transform has coordinates given in  $f_D$ , the  $d_{\text{eff},1}$  from our global fits is used to convert to mas on the sky. For each value of  $\theta$  along the main arc, we measure the offset and phase of the brightest point in  $\theta_{\perp}$ . This approach is similar to the back-mapped astrometry described in [Brisken et al. \(2010\)](#). The results are shown in Fig. 10. As we get to larger values of  $\theta_{\perp}$ , our signal to noise ratio per point drops and so we see a larger spread in the peak position as well as variations from our phase gradient. For  $\theta_{\parallel}$  between -15 and 15 mas, 95 percent of

measured peaks fall within 0.24 mas of the major axis suggesting an axial ratio of greater than 60.

To examine individual images directly from VLBI, 165 isolated peaks along or near the main arc were identified by eye from the frequency averaged  $\theta$ - $\theta$  diagram. The average phase in a small region about each point was measured for the ARGB and ARJB cross conjugate wavefields in each of the 2MHz subbands in order to measure its relative astrometric position. The average position and standard error for each of these points is shown in Fig. 11. As noted in [Brisken et al. \(2010\)](#), the back-mapped astrometric positions scatter less than those from VLBI phase measurements. Errors on the VLBI positions are on the order of 0.6 mas which makes them too large to detect the variations on the order of 0.2 mas seen from the back-mapping.

A crucial difference in our astrometric results compared to [Brisken et al. \(2010\)](#) is that the location of the millisecond feature is in the upper left quadrant as opposed to the lower left. In fact, all images have been mirrored in both right ascension and declination. This picture with the millisecond feature in the north is consistent with the monitoring results of [Zhu et al. \(in prep\)](#) who see the time delay of the feature decreasing during this epoch suggesting that the pulsar (moving almost due north) is approaching the feature. One possible explanation for this flip is that the choice of Fourier transform convention used to generate the spectra from baseband data can result in producing the complex conjugate of the visibilities, which in turn results in a mirroring of the VLBI images.  $\theta$ - $\theta$  allows us to make an additional test of the visibilities in cases such as this where a comparison of the response functions from single dish recovery can be compared to the results from visibilities alone. As seen in Fig. 2, when the consistent choice of visibility conjugation is chosen each dish sees only a constant phase offset between the two methods. However, when the complex conjugate of the visibility is used to make the  $\theta$ - $\theta$  matrix axes corresponding to the two dishes are reversed and the comparison will now produce a phase gradient determined by the time delay between the two dishes.

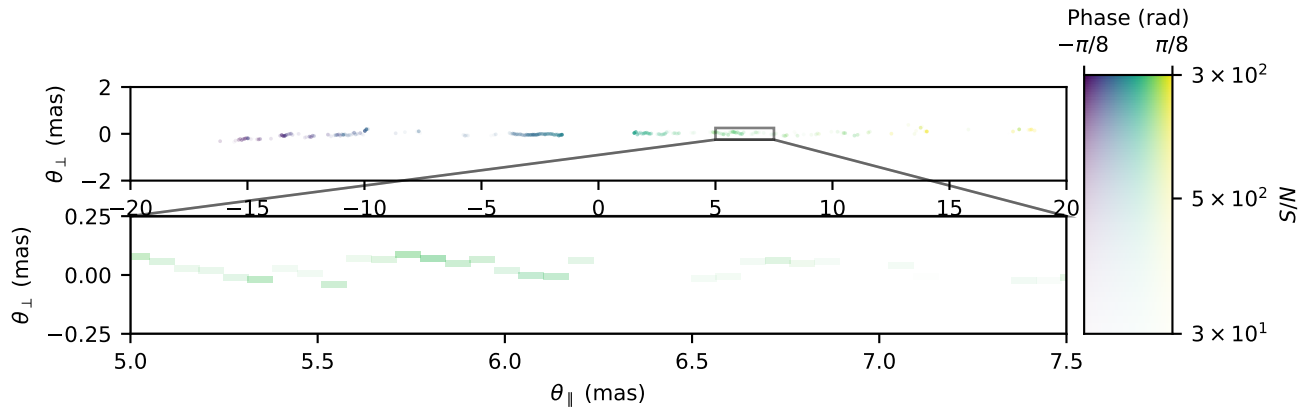


**Figure 10.** Offset of peak brightness perpendicular to the arc ( $\theta_{\perp}$ ) as a function of distance along the major axis of the lens ( $\theta_{\parallel}$ ). The lens is extremely anisotropic with an axial ratio greater than 60. The colour scale shows the residual phase of these points after removing our best fit gradient.

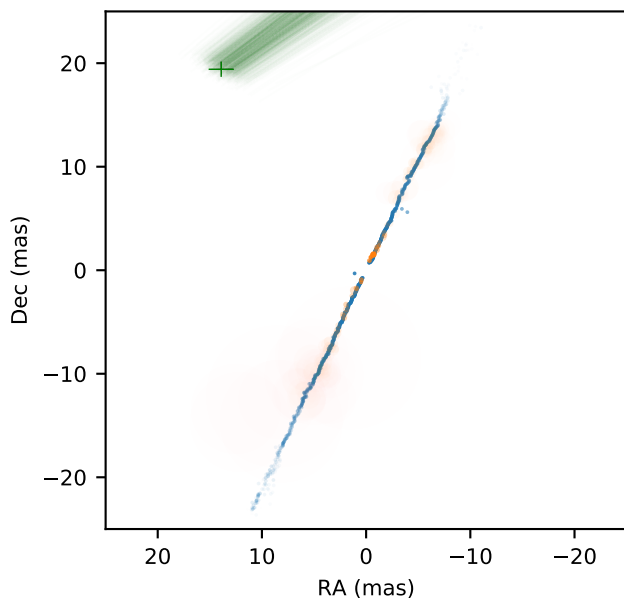


**Figure 11.** VLBI positions of 165 images along the main arc (orange) and the offsets measured from the frequency averaged  $\theta$ - $\theta$  along the screen direction measured in Sec. 5 (blue). With the relative brightness of points indicated with opacity and the size of the orange points indicating the uncertainty on the VLBI image position. The millisecond feature is shown in green with errorbars for the point of closest approach and probability of the line of images passing through each point shown with opacity.

## 7 RAMIFICATIONS

Using new  $\theta$ - $\theta$  techniques, we are able to measure the effective distance to the two screens seen for PSR B0834+06 to be  $1.186 \pm 0.005$  kpc and  $1.41 \pm 0.14$  kpc for the main arc and millisecond feature respectively. For the main arc, our results are consistent with the  $1.171 \pm 0.023$  kpc reported by [Briskin et al. \(2010\)](#). They also measure a slightly larger distance to the millisecond feature, but as it is within one sigma of the main arc effective distance they conclude the lenses are at the same distance. Our results expand this difference to the two sigma level.

The success at retrieving the dynamic wavefields from all dishes

in this well understood case also serves as a template for future work. Of particular interest is the potential to apply these methods to Earth-Space baselines such as RadioAstron. A natural starting ground for this would be archival data of PSR B0834+06 as described in [Smirnova et al. \(2020\)](#). The observations taken in 2015 offer the most promising path as they include more ground stations which improves the ability of  $\theta$ - $\theta$  methods to recover the wavefield of the low signal to noise RadioAstron data. The projected baseline for RadioAstron to Arecibo is approximately eighty times longer than Arecibo to Green Bank. The resulting increase in resolving power should allow us to improve our VLBI astrometry precision to below the 0.2mas level deviations indicated by the back-mapping.

## ACKNOWLEDGEMENTS

We acknowledge the support of the Natural Sciences and Engineering Research Council of Canada (NSERC), [funding reference number RGPIN-2019-067, 523638-201]. We receive support from Ontario Research Fund—research Excellence Program (ORF-RE), Simons Foundation, Canadian Institute for Advanced Research (CIFAR), and Alexander von Humboldt Foundation. The Arecibo Observatory is operated by SRI International under a cooperative agreement with the National Science Foundation (AST-1100968), and in alliance with Ana G. Méndez-Universidad Metropolitana, and the Universities Space Research Association. The National Radio Astronomy Observatory is a facility of the National Science Foundation operated under cooperative agreement by Associated Universities, Inc. Computations were performed on the Niagara supercomputer at the SciNet HPC Consortium. SciNet is funded by: the Canada Foundation for Innovation; the Government of Ontario; Ontario Research Fund - Research Excellence; and the University of Toronto. This research made use of Astropy,<sup>1</sup> a community-developed core Python package for Astronomy [Astropy Collaboration et al. \(2013\)](#); [Price-Whelan et al. \(2018\)](#).

<sup>1</sup> <http://www.astropy.org>

**DATA AVAILABILITY**

The code used in generating  $\theta$ - $\theta$  diagrams as well as fitting for curvatures can be found as part of the scintools python package originally developed by Daniel Reardon at [github.com/danielreardon/scintools](https://github.com/danielreardon/scintools) (Reardon et al. (2020)).

**REFERENCES**

- Astropy Collaboration et al., 2013, *A&A*, **558**, A33
- Baker D., Brisken W., van Kerkwijk M. H., Main R., Pen U.-L., Sprenger T., Wucknitz O., 2021, *Monthly Notices of the Royal Astronomical Society*, **510**, 4573
- Brisken W. F., Macquart J. P., Gao J. J., Rickett B. J., Coles W. A., Deller A. T., Tingay S. J., West C. J., 2010, *ApJ*, **708**, 232
- Liu S., Pen U.-L., Macquart J. P., Brisken W., Deller A., 2016, *MNRAS*, **458**, 1289
- Main R. A., et al., 2020, *Monthly Notices of the Royal Astronomical Society*, **499**, 1468
- Pen U.-L., Levin Y., 2014, *Monthly Notices of the Royal Astronomical Society*, **442**, 3338–3346
- Price-Whelan A. M., et al., 2018, *AJ*, **156**, 123
- Reardon D. J., et al., 2020, *ApJ*, **904**, 104
- Simard D., Pen U.-L., 2018, *Monthly Notices of the Royal Astronomical Society*, **478**, 983–994
- Simard D., Pen U.-L., Marthi V. R., Brisken W., 2019, *Monthly Notices of the Royal Astronomical Society*, **488**, 4963–4971
- Smirnova T. V., et al., 2020, *MNRAS*, **496**, 5149
- Sprenger T., Wucknitz O., Main R., Baker D., Brisken W., 2020, *Monthly Notices of the Royal Astronomical Society*, **500**, 1114
- Stinebring D. R., McLaughlin M. A., Cordes J. M., Becker K. M., Goodman J. E. E., Kramer M. A., Sheckard J. L., Smith C. T., 2001, *ApJ*, **549**, L97
- Walker M. A., Stinebring D. R., 2005, *MNRAS*, **362**, 1279
- Zhu Z., Johnson M. D., Narayan R., 2019, *ApJ*, **870**, 6

This paper has been typeset from a  $\text{\TeX}/\text{\LaTeX}$  file prepared by the author.